Supplementary Information

Non-linear spin correlation to intermediates in enhanced electrochemical nitrate reduction under magnetic fields

Dongsheng Shao,†[a,b] Qian Wu,†[a] Yuwei Zhang,†[a] Xiyang Cai,[a] Chencheng Dai,[a] Siyuan Zhu,[a] Fanxu Meng,[a] Pengfei Song,[a] Xiaoning Li,[b] Xiaoming Ren,[c] Tianze Wu*[a] and Zhichuan J. Xu*[a,d]

[a] School of Materials Science and Engineering, Nanyang Technological University, 50 Nanyang Avenue, Singapore 639798 (Singapore)

[b] Centre for Atomaterials and Nanomanufacturing (CAN), School of Science, RMIT University, Melbourne, Australia

[c] State Key Laboratory of Materials-Oriented Chemical Engineering and College of Chemistry and Molecular Engineering, Nanjing Tech University, Nanjing 211816 (China)

[d] The Centre of Advanced Catalysis Science and Technology, Nanyang Technological University, 50 Nanyang Avenue, Singapore 639798 (Singapore)

† These authors contributed equally: Dongsheng Shao, Qian Wu, Yuwei Zhang

* Corresponding authors.
E-mail address: xuzc@ntu.edu.sg (Z. Xu), tianze.wu@ntu.edu.sg (T. Wu)

This PDF file includes:

Supplementary text
Figs. S1 to S28
Tables S1 to S3

Supplementary text

Determination of nitrite

Nitrite concentration was quantified using UV-Vis spectrophotometry. The color reagent was prepared by dissolving 0.4 g of p-aminobenzenesulfonamide, 0.02 g of N-(1-naphthyl) ethylenediamine dihydrochloride and 1 mL of phosphoric acid in 5 mL of deionized water. For the measurement, 2.5 mL of the diluted electrolyte was mixed with 0.1 mL of color reagent, and after 40 minutes at room temperature, the absorption spectrum was recorded at 540 nm using a UV-vis spectrophotometer (UV-2700). Nitrite concentration was determined by comparison to a standard curve of ammonium chloride solutions.

Calculation of NO_2^- yield rate and FE

NO_2^- yield rate (ug h^{-1} cm^{-2}) = ($c_{NO_2^-}$ × V) / (t × S)

$FE_{NO_2^-}$ = (n × F × $c_{NO_2^-}$ × V) / ($M \times Q$) × 100 %

where $c_{NO_2^-}$ (μg mL^{-1}) is the measured nitrite concentration, V (mL) is the electrolyte volume in the cathodic compartment, t (h) is the electrochemical reduction time, S is the geometric surface area of WE, n is the number of electrons transferred (n = 2), F is the Faraday constant (96485 C mol^{-1}), M is the relative molecular mass of NO_2^- and Q (C) is the total charge of applied electricity.

^{15}N Isotope labeling experiment

To confirm the ammonia source, the ^{15}N isotopic labeled nitrate ($Na^{15}NO_3$, 99.99%) was used in the electrochemical reduction experiments. The electrolyte consisted of 0.5 M Na_2SO_4 and 0.1 M $Na^{15}NO_3$. After electrochemical reduction, 2 mL electrolyte with obtained $^{15}NH_4^+$-^{15}N was taken out and its pH was adjusted to 2 before analysis. 500 μl of sample solution and 56 μl of D_2O were mixed for the test by ^1H NMR (400 MHz). Similarly, the $^{14}NH_4^+$-^{14}N was tested by this method when $Na^{14}NO_3$ was used as a reactant. The ^1H NMR spectra of $^{15}NH_4^+$ and $^{14}NH_4^+$ showed typical double peaks and typical triple peaks, respectively.

In-situ ATR-FTIR tests

The in-situ ATR-FTIR tests were taken using a Bruker Vertex 80 instrument installed with an electrochemical VeeMax III apparatus from PIKE. A liquid nitrogen-cooled MCT detector was used. A Si prism evaporated with a 5 nm Ti layer and a 25 nm Au layer by an e-beam metal evaporator was used to reflect the signal at 60-degree angle. The catalysts were drop-casted onto the surface of the prism and used as WE. An Ag/AgCl (saturated KCl) and Pt wire served as RE and CE, respectively. The electrolyte of 0.5 M Na_2SO_4 + 0.1 M $NaNO_3$ was used. The in-situ spectra were recorded at various applied potentials.

Operando Raman tests

Operando Raman tests were performed on an i-Raman® Plus 785H Raman spectrometer with a laser wavelength of 785 nm. The catalyst was drop-cast onto a glassy carbon electrode as the WE, of which the plane was set perpendicular to the incident laser. An Ag/AgCl (saturated KCl) and Pt wire were used as RE and CE, respectively. The electrolyte of 0.5 M Na_2SO_4 + 0.1 M $NaNO_3$ was used. The spectrum was acquired under different potentials.

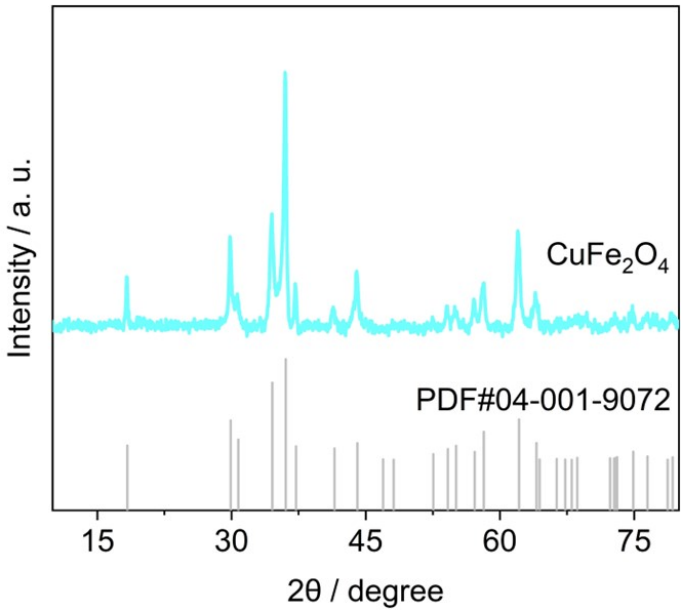

Fig. S1 PXRD pattern of as-prepared $CuFe_2O_4$ spinel oxide at ambient conditions.

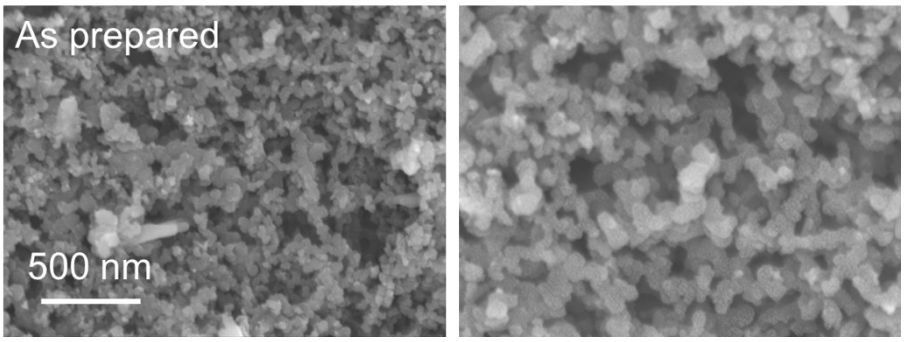

Fig. S2 FESEM images of as-prepared $CuFe_2O_4$ spinel oxide at the scale of 500 nm.

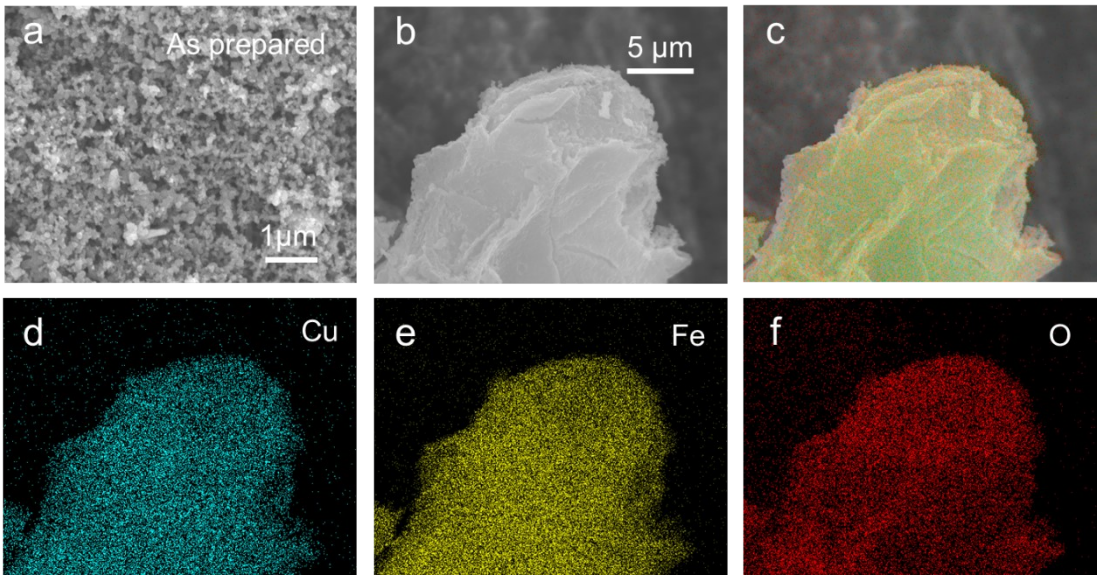

Fig. S3 FESEM images of the as-prepared $CuFe_2O_4$ spinel oxide at the scale of (a) 1µm, (b) 5µm. EDS mapping of $CuFe_2O_4$ for (c) Cu, Fe, and O, (d) Cu, (e) Fe, and (f) O elements.

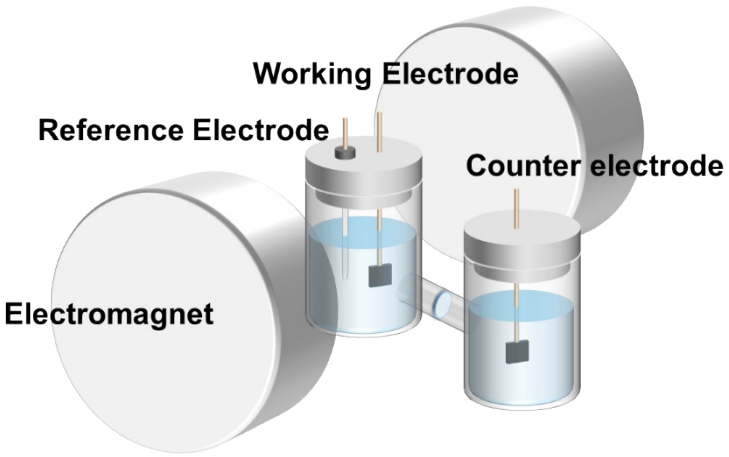

Fig. S4 Illustration of the experimental set-up under an external magnetic field during NO_3^-RR.

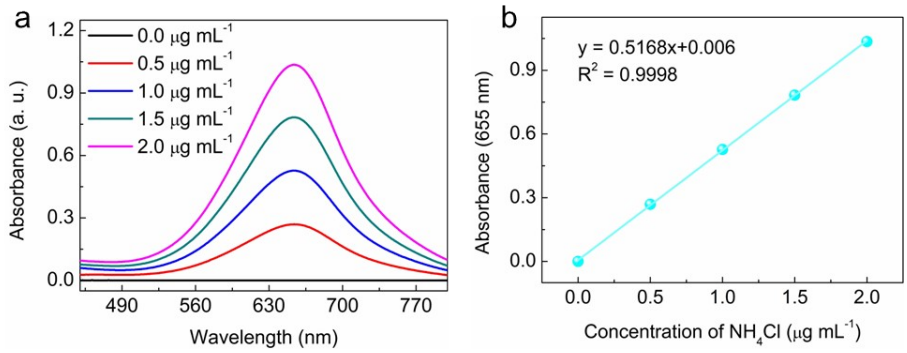

Fig. S5 UV-vis absorption spectra for different concentrations of ammonia-N (a) and the corresponding standard absorbance-ammonia concentration curve (b) NH_4Cl was used as ammonia-N sources for standard curve test.

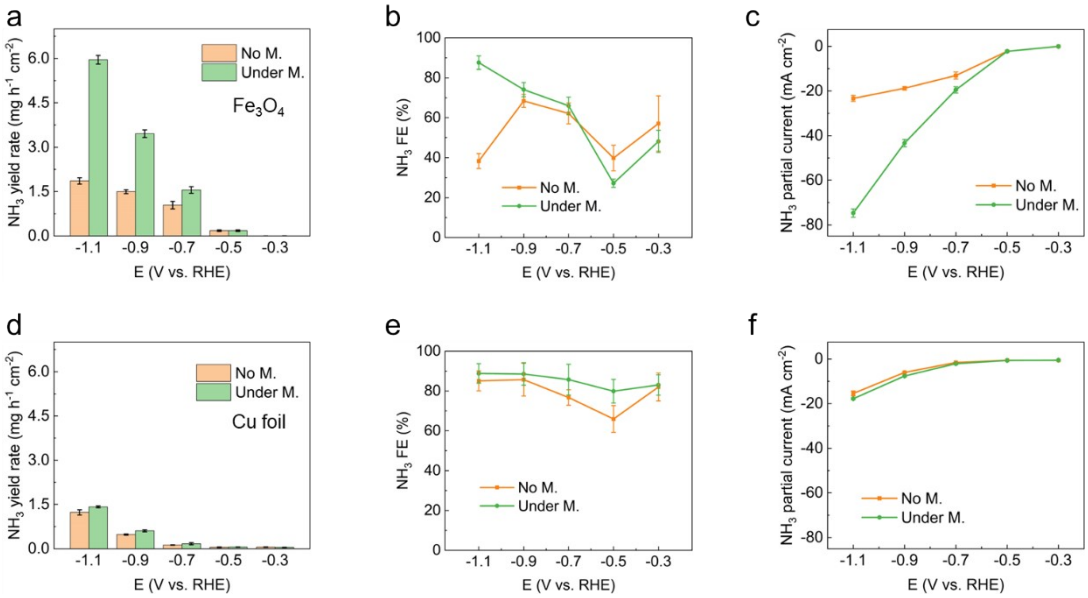

Fig. S6 NH_3 yield rate (a), NH_3 FE (b), and NH_3 partial current (c) of Fe_3O_4 with and without a constant magnetic field of 2500 Oe at various applied potentials. NH_3 yield rate (d), NH_3 FE (e), and NH_3 partial current (f) of Cu foil with and without a constant magnetic field of 2500 Oe at various applied potentials.

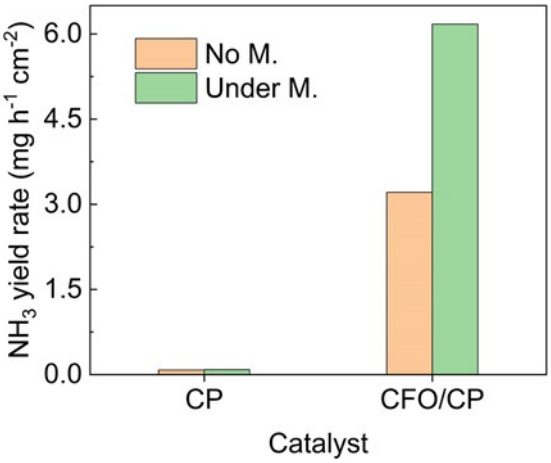

Fig. S7 Comparison of NH_3 yield rate on CP (Carbon paper) and CFO/CP ($CuFe_2O_4$ catalyst loading on the carbon paper) after electrocatalysis for 0.5h with and without a constant magnetic field of 2500 Oe at −1.1 V vs RHE.

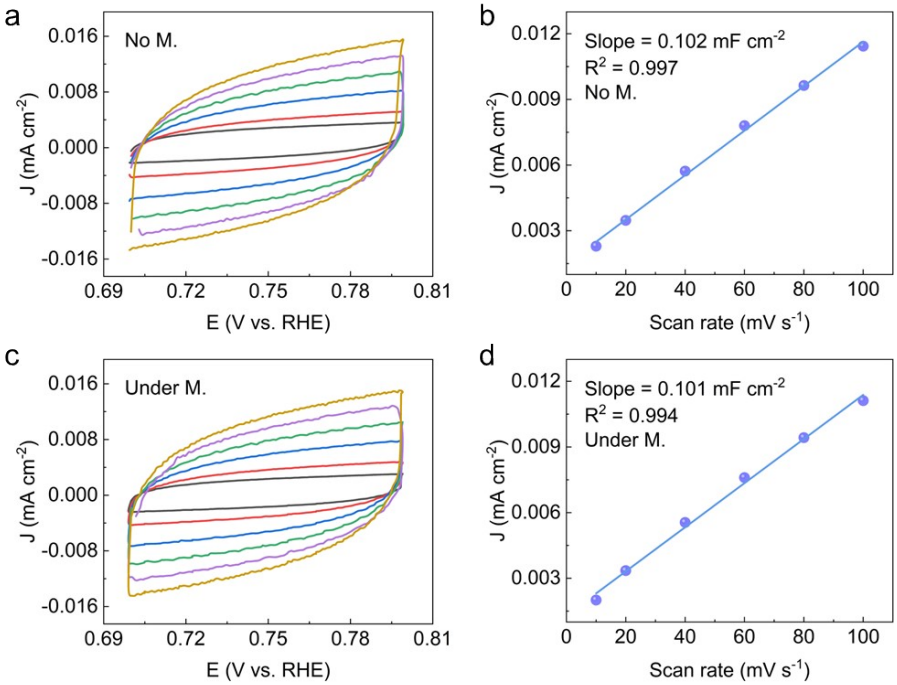

Fig. S8 CV curves of $CuFe_2O_4$ (a) without and (c) with a constant magnetic field of 2500 Oe at various scan rates of 10, 20, 40, 60, 80 and 100 mV s^{-1}. Plots of the current density versus the scan rate for $CuFe_2O_4$ (b) without and (d) with a constant magnetic field of 2500 Oe. The measured double-layer capacitances are determined to be 0.102 mF cm^{-2} for $CuFe_2O_4$ without magnetic field and 0.101 mF cm^{-2} for $CuFe_2O_4$ with magnetic field. Assuming the specific capacitance of the catalyst as 40 μF cm^{-2}, the electrochemical active surface area (ECSA) of $CuFe_2O_4$ without and with magnetic field are calculated as 2.55 and 2.525 cm^2_{ECSA}, respectively.

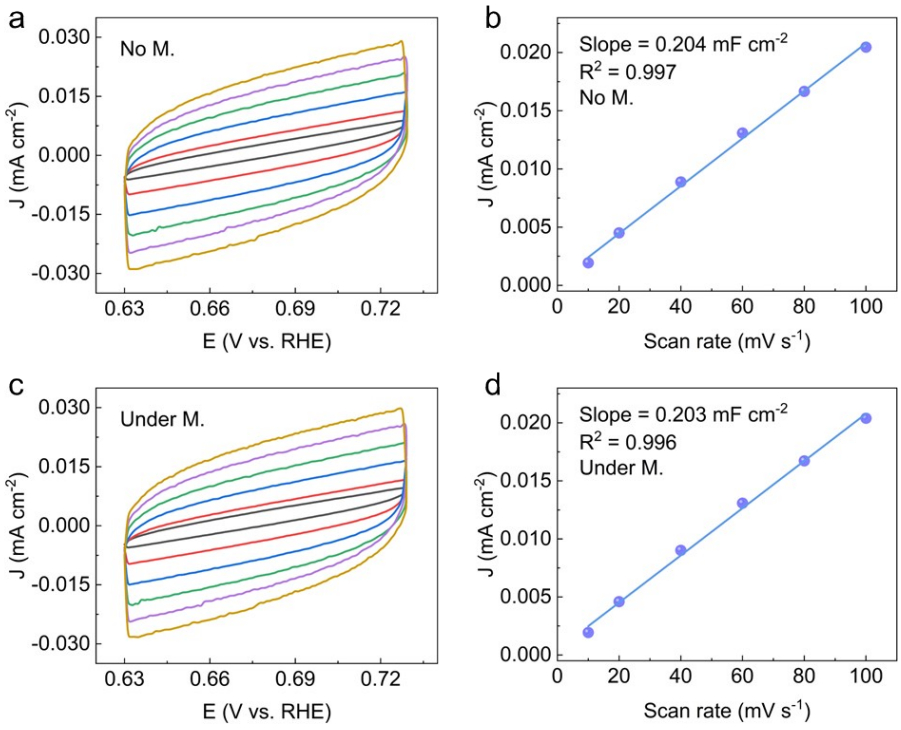

Fig. S9 CV curves of Fe_3O_4 (a) without and (c) with a constant magnetic field of 2500 Oe at various scan rates of 10, 20, 40, 60, 80 and 100 mV s^{-1}. Plots of the current density versus the scan rate for Fe_3O_4 (b) without and (d) with a constant magnetic field of 2500 Oe. The measured double-layer capacitances are determined to be 0.204 mF cm^{-2} for Fe_3O_4 without magnetic field and 0.203 mF cm^{-2} for Fe_3O_4 with magnetic field. The ECSA of Fe_3O_4 without and with magnetic field are calculated as 5.1 and 5.075 cm^2_{ECSA}, respectively.

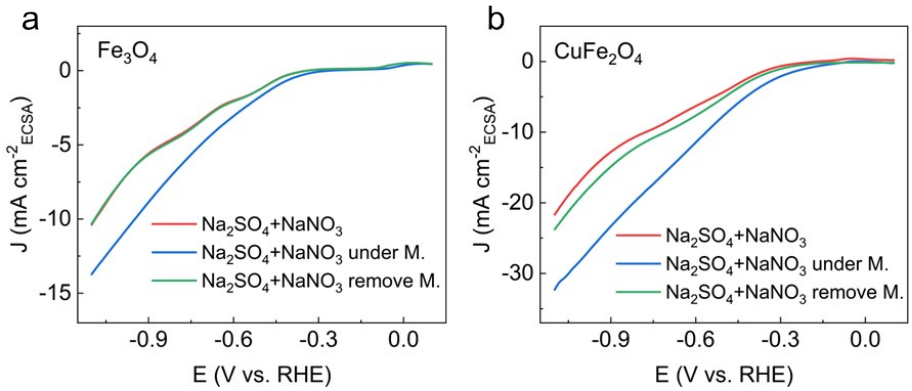

Fig. S10 The LSV curves of (a) Fe_3O_4 and (b) $CuFe_2O_4$ from Figs. S8 and S9 normalized to the ECSA.

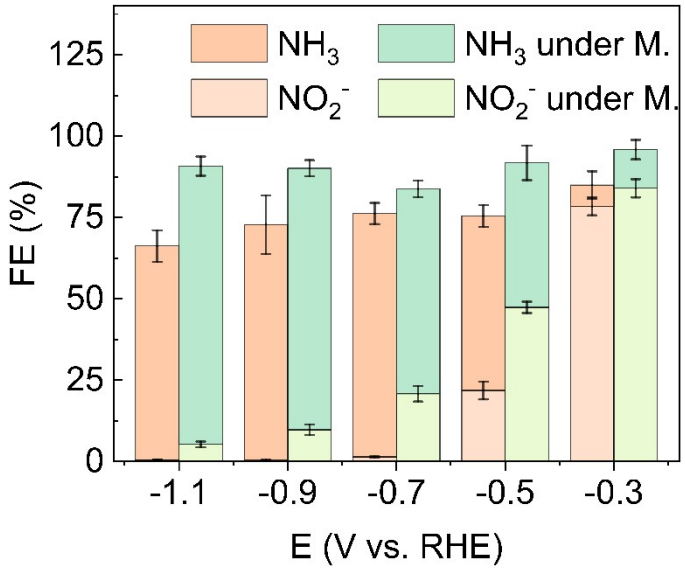

Fig. S11 NH_3 FE and NO_2^- FE of $CuFe_2O_4$ without and with an external magnetic field of 2500 Oe at various applied potentials.

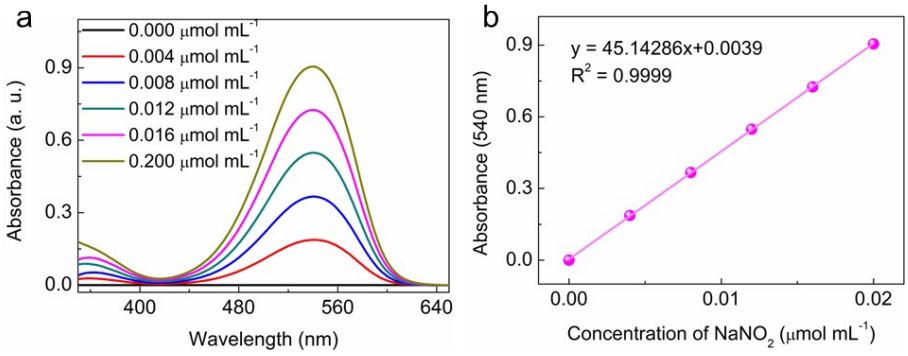

Fig. S12 UV-vis absorption spectra for different concentrations of nitrite-N (a) and the corresponding standard absorbance-nitrite curve (b). $NaNO_2$ was used as nitrite-N source for standard curve test.

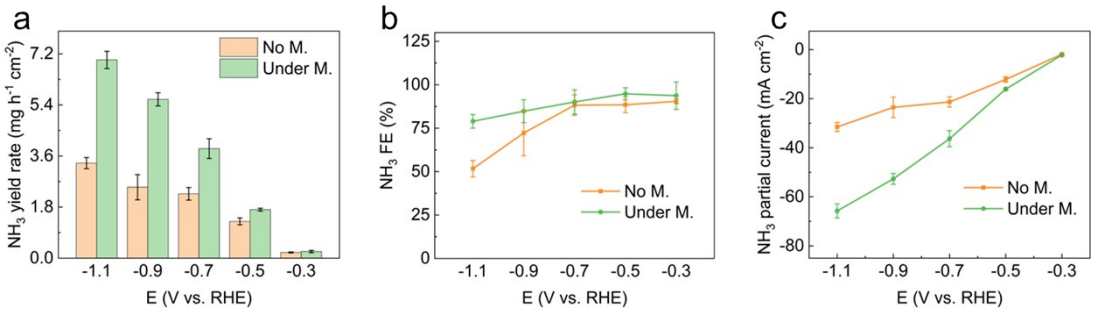

Fig. S13 NH_3 yield rate (a), NH_3 FE (b), and NH_3 partial current (c) of $CuFe_2O_4$ with and without a constant magnetic field of 2500 Oe at various applied potentials during the nitrite reduction reaction.

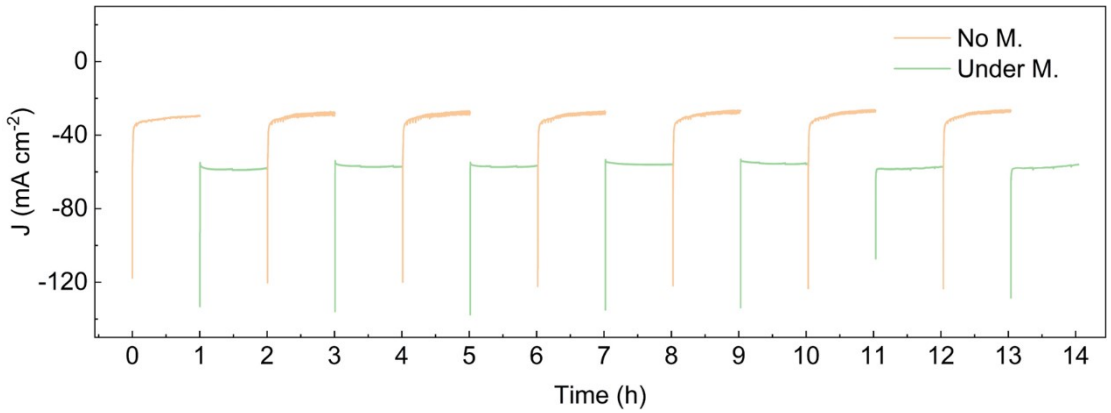

Fig. S14 CA curves of $CuFe_2O_4$ at −0.9 V vs. RHE during 14 cycles of alternating electrolysis, with and without a constant magnetic field of 2500 Oe.

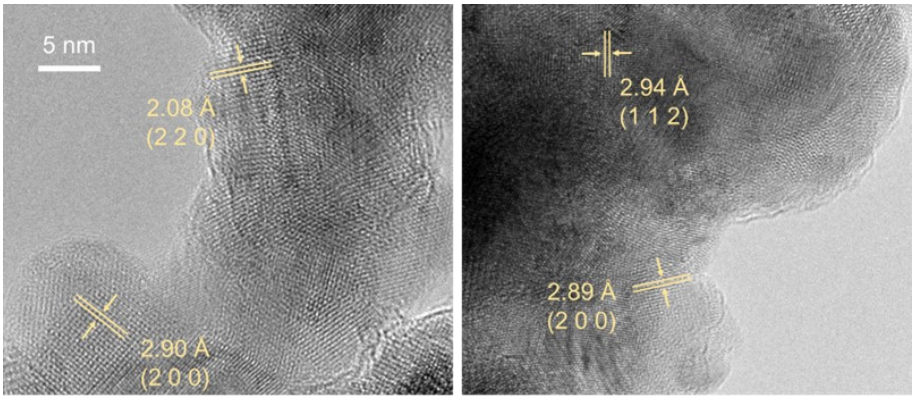

Fig. S15 HRTEM images of $CuFe_2O_4$ after NO_3^-RR.

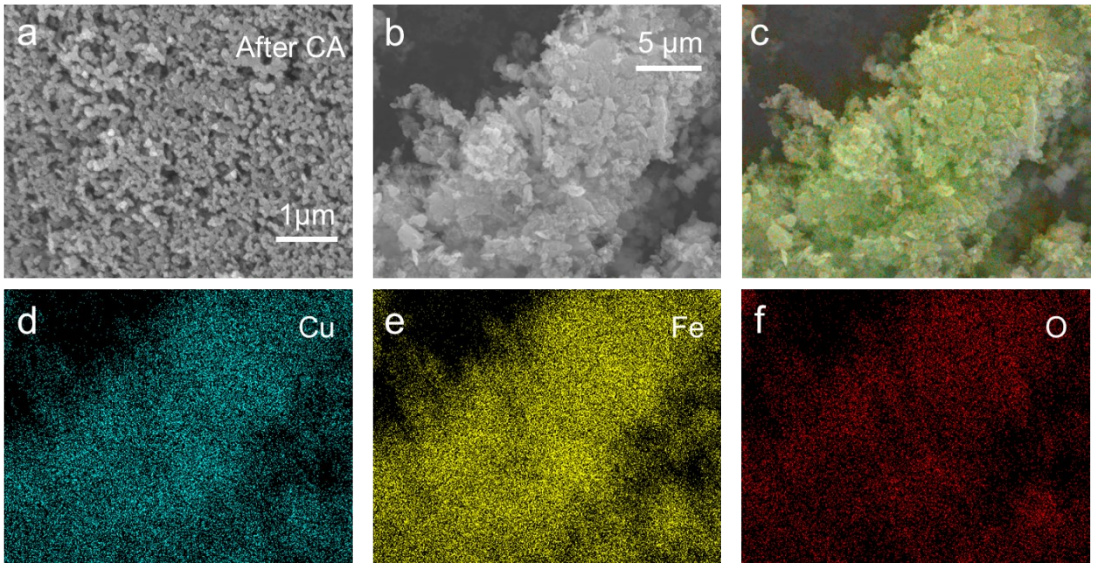

Fig. S16 FESEM images of $CuFe_2O_4$ after CA at the scale of (a) 1µm, (b) 5µm. EDS mapping of $CuFe_2O_4$ for (c) Cu, Fe, and O, (d) Cu, (e) Fe, and (f) O elements.

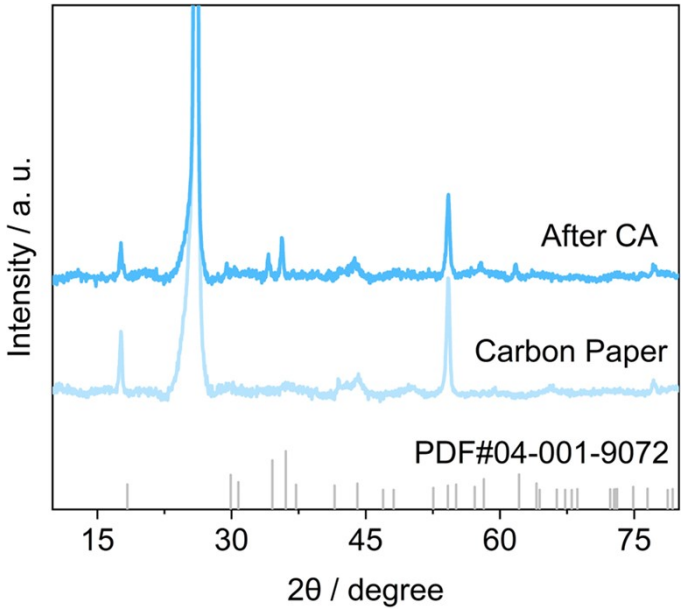

Fig. S17 PXRD patterns of $CuFe_2O_4$ spinel oxide loading on carbon paper after NO_3^-RR at ambient conditions.

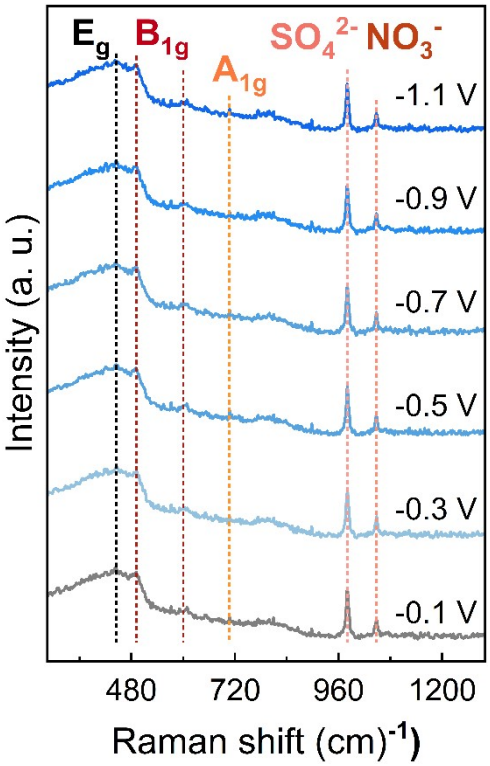

Fig. S18 Operando Raman spectra of $CuFe_2O_4$ at different potentials from −0.1 V to −1.1 V vs RHE in 0.5 M Na_2SO_4 + 0.1 M $NaNO_3$.

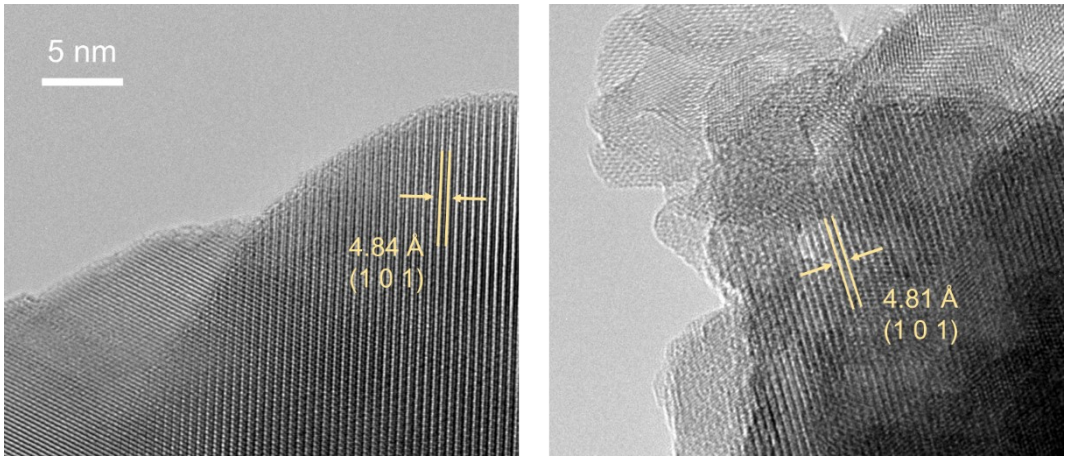

Fig. S19 HRTEM images of $CuFe_2O_4$ before and after NO_3^-RR.

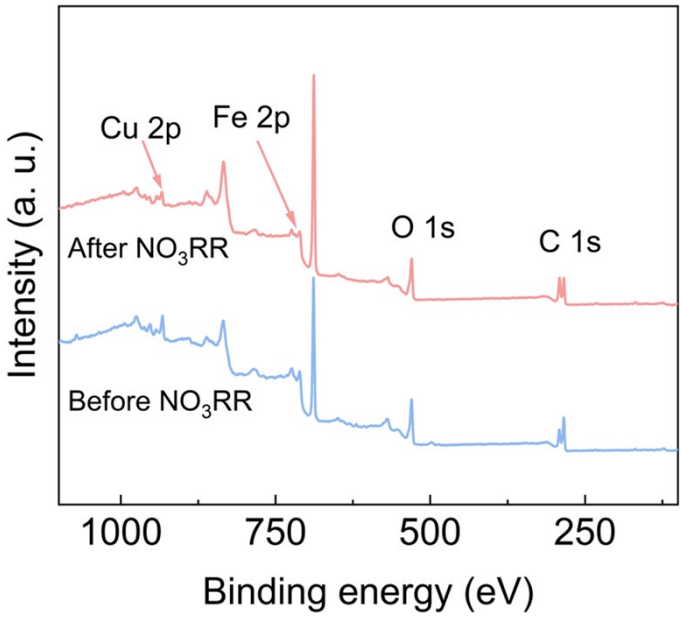

Fig. S20 XPS spectra of $CuFe_2O_4$ before and after NO_3^-RR.

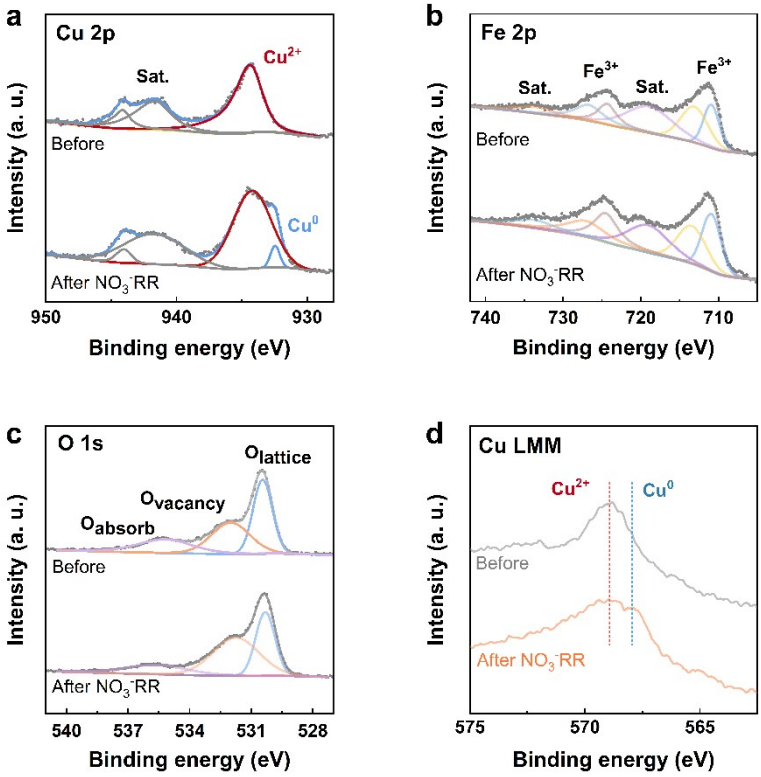

Fig. S21 Cu 2p XPS spectra (a), Fe 2p XPS spectra (b), O 1s XPS spectra (c) and Cu LMM AES spectra (d) of $CuFe_2O_4$ before and after NO_3^-RR.

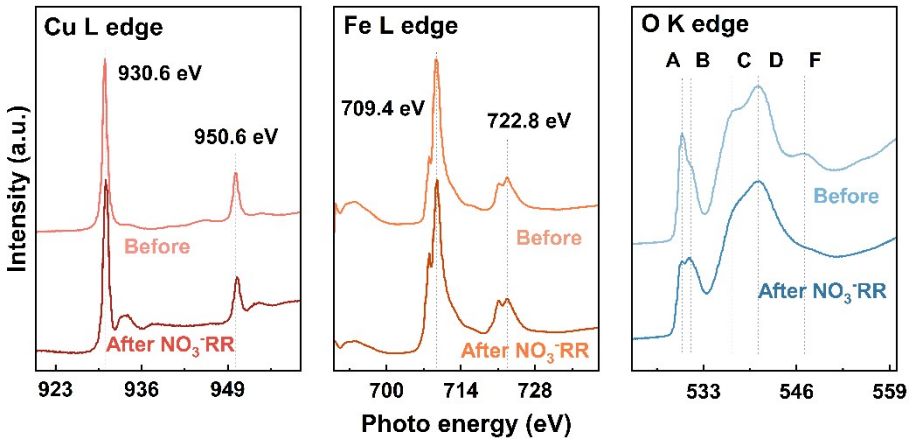

Fig. S22 The XAS spectrum of Cu L-edge, Fe L-edge, O K-edge of $CuFe_2O_4$ before and after NO_3^-RR.

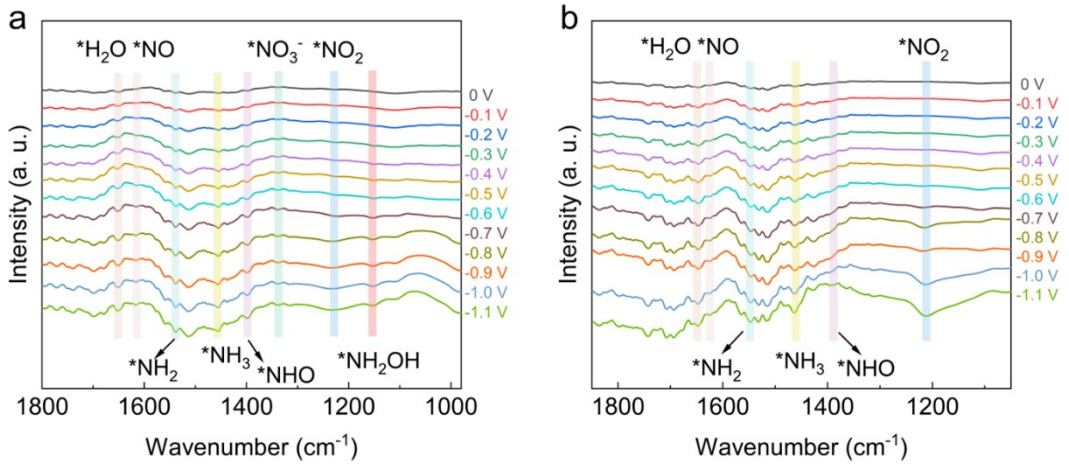

Fig. S23 The in-situ ATR-FTIR spectra of $CuFe_2O_4$ in the electrolyte of (a) 0.5 M Na_2SO_4 + 0.1 M $NaNO_3$ and (b) 0.5 M Na_2SO_4 + 0.1 M $NaNO_2$ at various potentials.

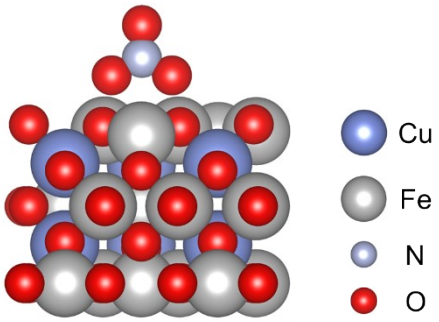

Fig. S24 The corresponding structure of *NO_3 absorbed on the Fe/Fe site of $CuFe_2O_4$.

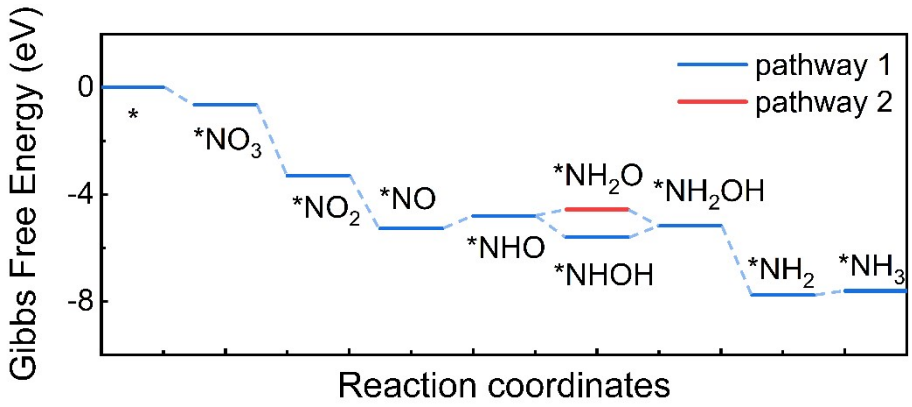

Fig. S25 Free energy diagrams of individual intermediates on $CuFe_2O_4$ and the corresponding structure of intermediates during the nitrate reduction reaction.

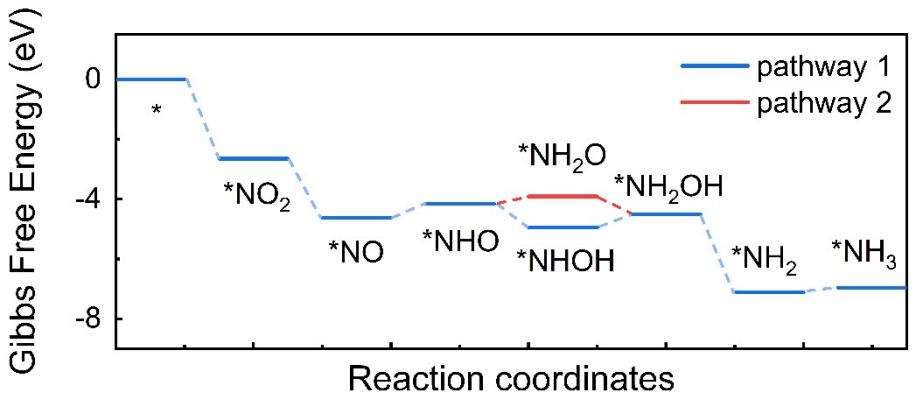

Fig. S26 Free energy diagrams of individual intermediates on $CuFe_2O_4$ and the corresponding structure of intermediates during the nitrite reduction reaction.

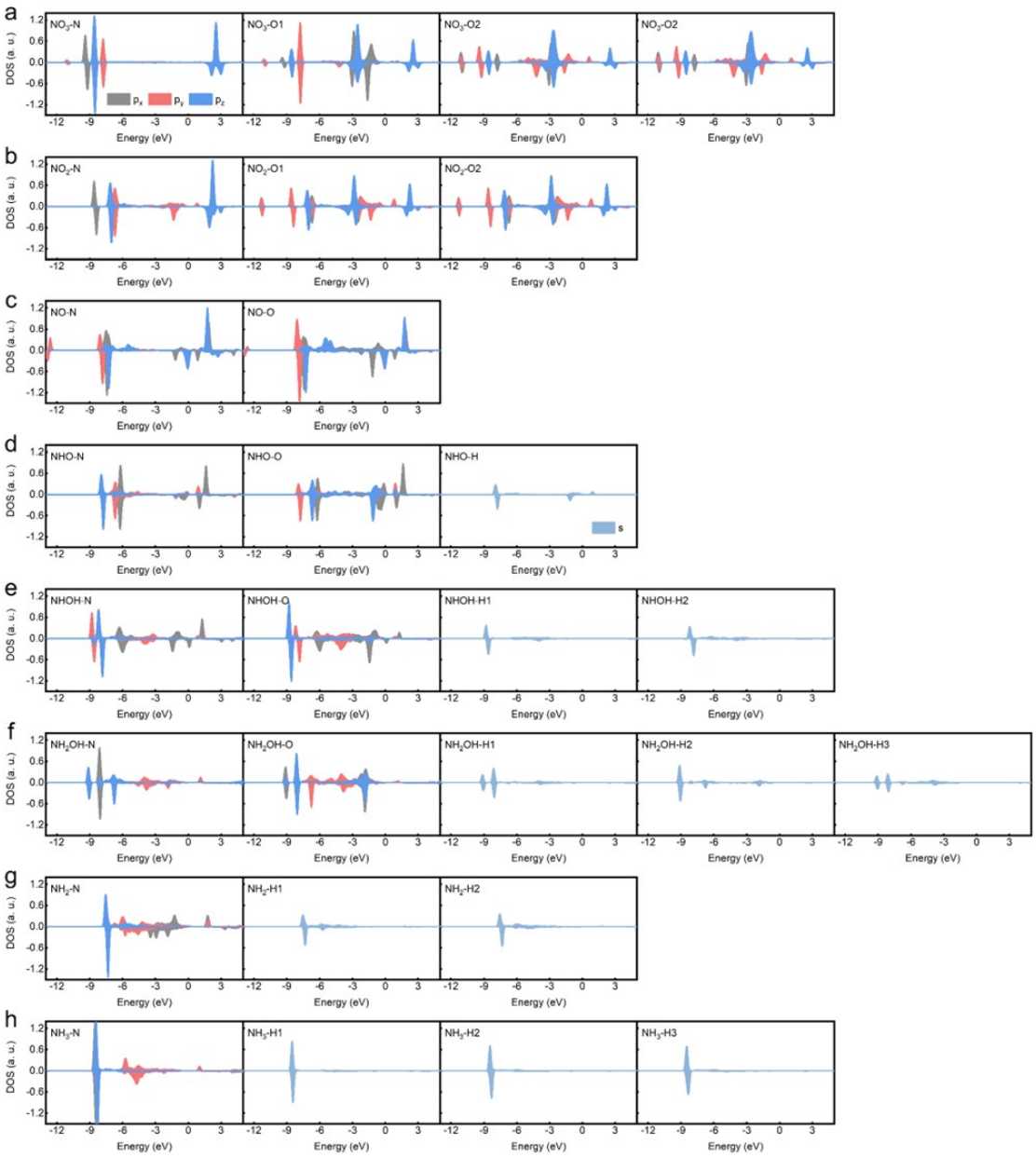

Fig. S27 DOSs for all atoms of intermediates involved in the NO_3^-RR process, including (a) *NO_3, (b) *NO_2, (c) *NO, (d) *NHO, (e) *NH_2O, (f) *NH_2OH, (g) *NH_2 and (h) *NH_3.

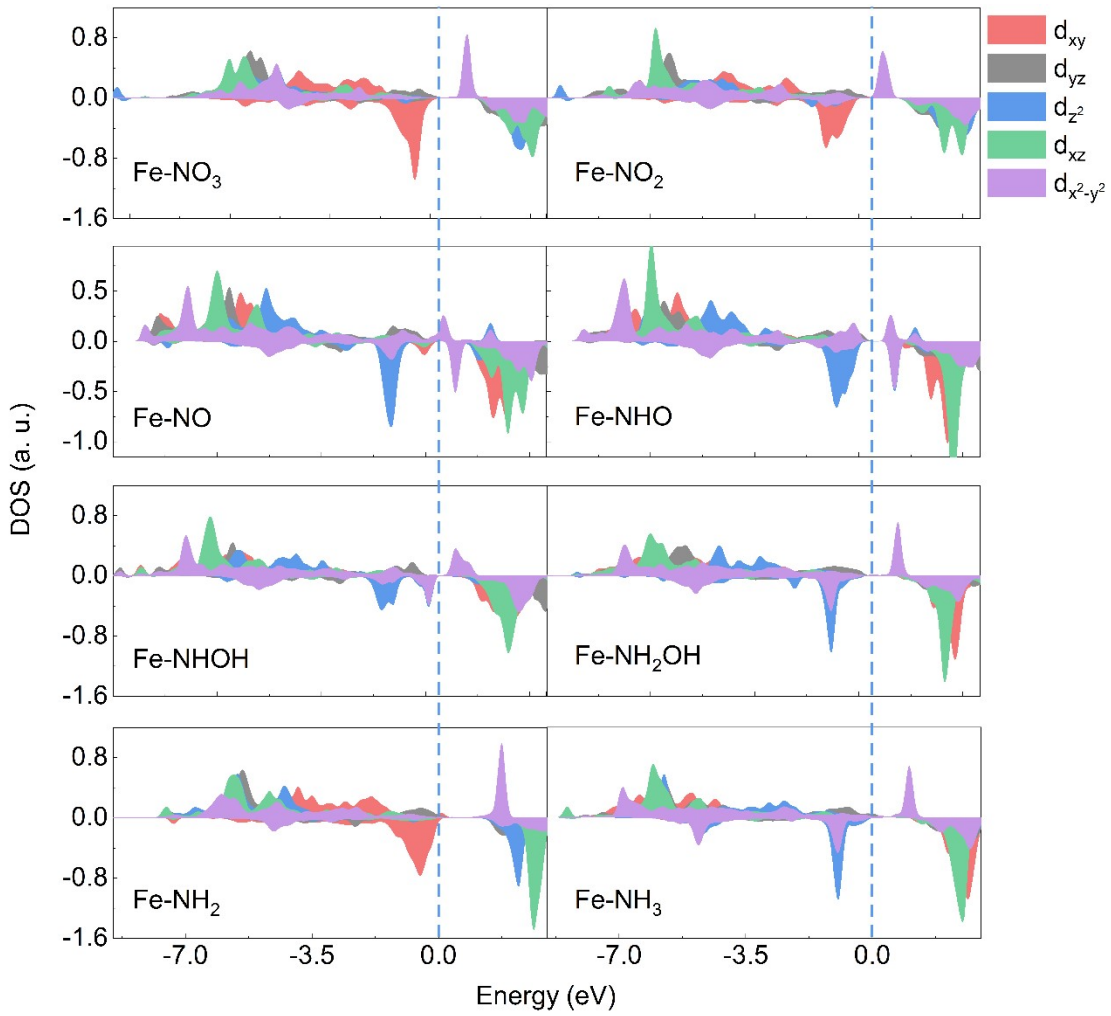

Fig. S28 DOSs of Fe atom on $CuFe_2O_4$ after NO_3, NO_2, NO, NHO, NH_2O, NH_2OH, NH_2 and NH_3 adsorption.

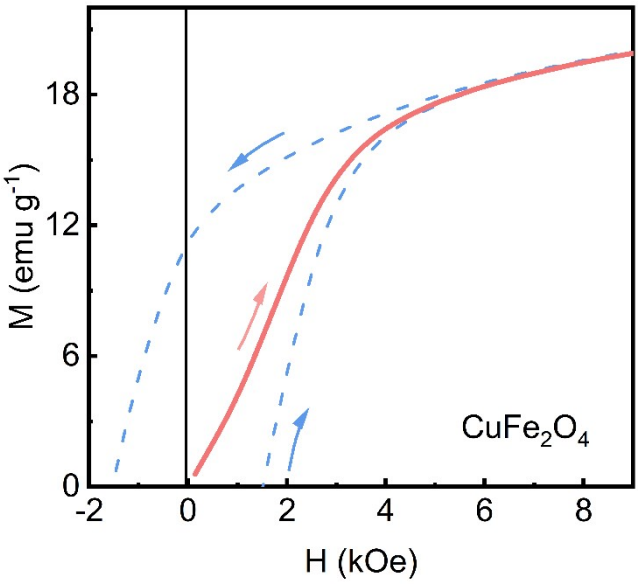

Fig. S29 Magnetic hysteresis loops of $CuFe_2O_4$ at room temperature.

Table S1: Comparison of the NH_3 yield rate defined by the electrode area among various electrodes.

Catalysts	electrolyte	NH_3 yield rate ($mg\ h^{-1}\ cm^{-2}$)	FE_{NH3}	Potential (vs. RHE)	ref
$CuFe_2O_4$	0.5M Na_2SO_4 + 0.1M $NaNO_3$	5.97	85.5%	–1.1 V	This work
Fe_3O_4	0.5M Na_2SO_4 + 0.1M $NaNO_3$	5.96	87.6%	–1.1 V	This work
Fe/Cu-NG	1 M KOH + 0.1 M KNO_3	4.41	~92.51%	–0.3 V	1
Fe single atom	0.1 M K_2SO_4 + 0.5 M KNO_3	2.05	~75%	–0.66 V	2
Fe-PPy SACs	0.1 M KOH + 0.1 M KNO_3	2.72	99.69%	–0.3	3
Fe_2TiO_5	PBS solution + 0.1M $NaNO_3$	1.24	87.6%	–0.9	4
SA-Fe(II)	0.5 M Na_2SO_4 + 0.1 M PBS+ 0.2 M $NaNO_3$	4.93	99.6%	–1.0	5
$CuCl/TiO_2$	0.5 M Na_2SO_4 + 100 ppm KNO_3	2.21	85%	–0.8	6
Cu–PTCDA	0.1 M PBS + 500 ppm KNO_3	0.44	77%	–0.4	7
Co–Fe@Fe_2O_3	0.1 M Na_2SO_4 + 50 ppm $NaNO_3$	1.51	85.2%	–0.75	8
defective CuO	0.05 M H_2SO_4 + 0.05 M KNO_3	5.61	45%	–0.7	9
Cu49Fe1	0.1 M K_2SO_4 + 200 ppm KNO_3	3.91	94.5%	–0.74	10

Cu/Cu_2O	0.5 M Na_2SO_4 + 200 ppm $NaNO_3$	4.17	95.8%	–0.85	11
TiO_{2-x}	0.5 M Na_2SO_4 + 50 ppm $NaNO_3$	0.77	85%	–0.95	12
Co/CoO NSAs	0.1 M Na_2SO_4 + 200 ppm $NaNO_3$	3.23	93.8%	–0.65	13
Cu single-atom	0.5 M Na_2SO_4 + 1000 ppm KNO_3	28.73	70%	–2.0	14
Cu-N-C SAC	0.1 M KOH + 0.1 M KNO_3	4.5	84.7%	–1.0	15

Table S2: Comparison of the NH_3 and NO_2^- yield rate at −1.1 V vs RHE under gradient magnetic field.

Magnetic field (Oe)	NH_3 yield rate ($mg\ h^{-1}\ cm^{-2}$)	Standard deviation	NO_2^- yield rate ($mg\ h^{-1}\ cm^{-2}$)	Standard deviation
0	2817.40	130.68	205.00	31.88
500	3589.09	254.93	315.19	23.98
1000	5100.50	165.14	819.14	245.60
1500	5433.84	49.39	1995.58	338.25
2000	5703.24	207.45	3536.61	264.59
2500	6022.88	217.46	4693.60	288.19

Table S3: Comparison of the NH_3 and NO_2^- FE at −1.1 V vs RHE under gradient magnetic field.

Magnetic field (Oe)	NH_3 FE (%)	Standard deviation	NO_2^- FE (%)	Standard deviation
0	61.95	3.41	0.42	0.08
500	72.36	1.40	0.59	0.03
1000	85.28	2.30	1.26	0.35
1500	81.29	1.86	2.76	0.51
2000	84.11	1.42	4.83	0.48
2500	86.12	3.69	6.20	0.46

References

1. S. Zhang, J. Wu, M. Zheng, X. Jin, Z. Shen, Z. Li, Y. Wang, Q. Wang, X. Wang, H. Wei, J. Zhang, P. Wang, S. Zhang, L. Yu, L. Dong, Q. Zhu, H. Zhang and J. Lu, *Nat. Commun.* 2023, **14**, 3634.
2. Z. Y. Wu, M. Karamad, X. Yong, Q. Huang, D. A. Cullen, P. Zhu, C. Xia, Q. Xiao, M. Shakouri, F. Y. Chen, J. Y. (Timothy) Kim, Y. Xia, K. Heck, Y. Hu, M. S. Wong, Q. Li, I. Gates, S. Siahrostami and H. Wang, *Nat. Commun.* 2021, **12**, 2870.
3. P. Li, Z. Jin, Z. Fang and G. Yu, *Energy Environ. Sci.* 2021, **14**, 3522–3531.
4. H. Du, H. Guo, K. Wang, X. Du, B. A. Beshiwork, S. Sun, Y. Luo, Q. Liu, T. Li and X. Sun, *Angew. Chem. Int. Ed.* 2023, **62**, 202215782.
5. C. Liu, G. Zhang, W. Zhang, Z. Gu and G. Zhu, *Proc. Natl. Acad. Sci.* 2023, **120**, e2209979120.
6. W. J. Sun, H. Q. Ji, L. X. Li, H. Y. Zhang, Z. K. Wang, J. H. He and J. M. Lu, *Angew. Chem. Int. Ed.* 2021, **60**, 22933.
7. G. F. Chen, Y. Yuan, H. Jiang, S. Y. Ren, L. X. Ding, L. Ma, T. Wu, J. Lu and H. Wang, *Nat. Energy* 2020, **5,** 605–613.
8. S. Zhang, M. Li, J. Li, Q. Song and X. Liu, *Proc. Natl. Acad. Sci.* 2022, **119**, e2115504119.
9. R. Daiyan, T. Tran-Phu, P. Kumar, K. Iputera, Z. Tong, J. Leverett, M. H. A. Khan, A. A. Esmailpour, A. Jalili, M. Lim, A. Tricoli, R.-S. Liu, X. Lu, E. Lovell and R. Amal, *Energy Environ. Sci.* 2021, **14**, 3588–3598.
10. C. Wang, Z. Liu, T. Hu, J. Li, L. Dong, F. Du, C. Li and C. Guo, *ChemSusChem* 2021, **14**, 1825–1829.
11. Y. Wang, W. Zhou, R. Jia, Y. Yu and B. Zhang, *Angew. Chem. Int. Ed.* 2020, **59**, 5350–5354.
12. R. Jia, Y. Wang, C. Wang, Y. Ling, Y. Yu and B. Zhang, *ACS Catal.* 2020, **10**, 3533–3540.
13. Y. Yu, C. Wang, Y. Yu, Y. Wang and B. Zhang, *Sci. China Chem.* 2020, **63**,

1469–1476.

14. X. F. Cheng, J. H. He, H. Q. Ji, H. Y. Zhang, Q. Cao, W. J. Sun, C. Yan and J. M. Lu, *Adv. Mater.* 2022, **34**, 2205767.
15. J. Yang, H. Qi, A. Li, X. Liu, X. Yang, S. Zhang, Q. Zhao, Q. Jiang, Y. Su, L. Zhang, J. F. Li, Z. Q. Tian, W. Liu, A. Wang and T. Zhang, *J. Am. Chem. Soc.* 2022, **144**, 12062–12071.